

A 600 kpc complex radio source at the center of Abell 3718 discovered by the EMU and POSSUM surveys

F. Loi¹, M. Brienza^{2,3,4}, C. J. Riseley^{3,4,5}, L. Rudnick⁶, W. Boschin^{7,8,9}, L. Lovisari^{2,10}, E. Carretti⁴, B. Koribalski^{5,11}, C. Stuardi^{3,4}, S. P. O'Sullivan¹², A. Bonafede^{3,4}, M. D. Filipović¹¹, A. Hopkins¹³.

¹ INAF–Osservatorio Astronomico di Cagliari, via della Scienza 3, Selargius, Italy
e-mail: francesca.loi@inaf.it

² INAF – OAS Osservatorio di Astrofisica e Scienza dello Spazio di Bologna, Via Gobetti 93/3, 40129, Bologna, Italia

³ Dipartimento di Fisica e Astronomia, Università degli Studi di Bologna, via P. Gobetti 93/2, 40129 Bologna, Italy

⁴ INAF – Istituto di Radioastronomia, via P. Gobetti 101, 40129 Bologna, Italy

⁵ Australia Telescope National Facility (ATNF), CSIRO Astronomy and Space Science, P.O. Box 76, Epping, NSW 1710, Australia

⁶ Minnesota Institute for Astrophysics, University of Minnesota, 116 Church St. SE, Minneapolis, MN 55455, USA

⁷ Fundación G. Galilei - INAF (Telescopio Nazionale Galileo), Rambla J. A. Fernández Pérez 7, E-38712 Breña Baja (La Palma), Spain

⁸ Instituto de Astrofísica de Canarias, C/Vía Láctea s/n, E-38205 La Laguna (Tenerife), Spain

⁹ Departamento de Astrofísica, Univ. de La Laguna, Av. del Astrofísico Francisco Sánchez s/n, E-38205 La Laguna (Tenerife), Spain

¹⁰ Center for Astrophysics | Harvard & Smithsonian, 60 Garden Street, Cambridge, MA 02138, USA

¹¹ School of Science, Western Sydney University, Locked Bag 1797, Penrith, NSW 2751, Australia

¹² School of Physical Sciences and Centre for Astrophysics & Relativity, Dublin City University, Glasnevin D09 W6Y4, Ireland

¹³ Australian Astronomical Optics, Macquarie University, 105 Delhi Rd, North Ryde, NSW 2113, Australia

Received December 7, 2022; accepted January **, ****

ABSTRACT

Context. Multifrequency studies of galaxy clusters are crucial for inferring their dynamical states and physics. Moreover, these studies allow us to investigate cluster-embedded sources, whose evolution is affected by the physical and dynamical condition of the cluster itself. So far, these kinds of studies have been preferentially conducted on clusters visible from the northern hemisphere due to the high-fidelity imaging capabilities of ground-based radio interferometers located there.

Aims. In this paper, we conducted a multifrequency study of the poorly known galaxy cluster Abell 3718. We investigated the unknown origin of an extended radio source with a length of ~ 612 kpc at 943 MHz detected in images from the Evolutionary Map of the Universe (EMU) and Polarisation Sky Survey of the Universe's Magnetism (POSSUM) surveys.

Methods. We analyzed optical and X-ray data to infer the dynamical state of the cluster and, in particular, the merger activity. We conducted a radio spectral index study from 943 MHz up to 9 GHz. We also evaluated the polarization properties of the brightest cluster-embedded sources to understand if they are related to the radio emission observed on larger scales.

Results. The cluster appears to be in a relaxed dynamical state, but there is clear asymmetry of the X-ray surface brightness distribution perpendicular to the direction of the largest angular extension of the radio source. The morphology of the cluster radio emission observed from 900 MHz to 9 GHz shows a system composed of a northern compact radio source and a southern radio galaxy whose jets are bent in the direction of an ultra-steep ($\alpha \approx 3.6$), thin (few tens of kpc) arc of radio emission between the first two radio sources. The spectral index gradient along the radio source and the polarization images at high frequency suggest that the thin arc is an extension of the southern radio galaxy, which may have been energized by interacting with the X-ray gas. An additional structure extending to the northwest from the southern radio galaxy may be an unusual truncated radio jet that either failed to expand or faded away due to energy losses. Deeper X-ray and radio observations are needed to better constrain the physics at play in this cluster.

Key words. galaxies: clusters: individual: Abell 3718 – galaxies: clusters: intracluster medium – surveys

1. Introduction

Galaxy clusters host an incredible realm of radio source diversity: star forming galaxies, radio galaxies, remnant radio galaxies, radio phoenixes, radio halos, radio relics, and mini-halos (see e.g., van Weeren et al. 2019, for the most recent review of the field). With the advent of the new generation of radio telescopes paving the way for the upcoming Square Kilometre Array (SKA), we are detecting ever more peculiar sources that challenge our historic taxonomy and provide new opportunities for understanding the complex physics at work in clusters (see e.g., Govoni et al. 2019; Botteon et al. 2020a,b; Biava et al. 2021;

Rudnick 2021; Riseley et al. 2022a). Indeed, the detection and the classification of cluster-embedded radio sources can provide crucial information about the evolution of both clusters and cluster galaxies and how the sources interact with the environment.

For instance, ram-pressure stripping phenomena on cluster galaxies are a well known example of how the intracluster medium (ICM) can dramatically change a galaxy's morphology and therefore its evolution, forming the so-called jellyfish galaxies (e.g. Smith et al. 2010; Fumagalli et al. 2014; Ebeling et al. 2014). Similarly, the interaction between active radio jets and

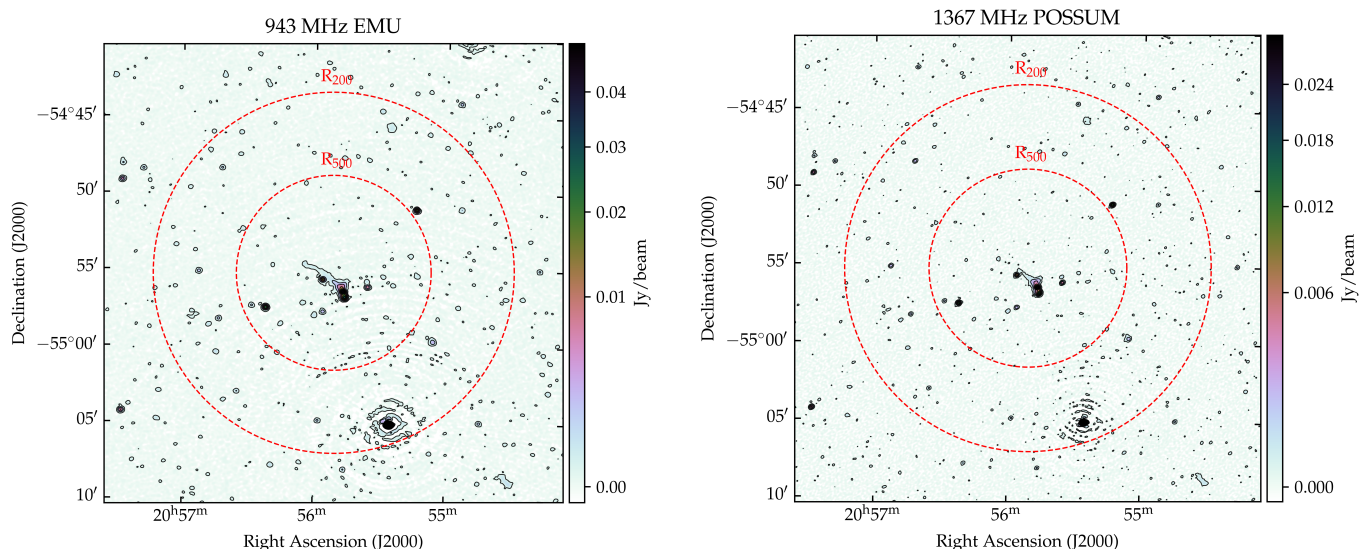


Fig. 1. ASKAP images of the galaxy cluster A3718. Left: 943 MHz EMU total intensity image. The beam size is 13.96×10.89 arcsec² and BPA = -58.15 deg. Right: 1.367 MHz POSSUM total intensity image. The beam size is 10.00×7.56 arcsec² and BPA = -54.63 deg. In both images contours start at 3σ and increase by a factor of $\sqrt{2}$ with σ equal to $40 \mu\text{Jy}/\text{beam}$ and $30 \mu\text{Jy}/\text{beam}$ in the EMU and POSSUM image, respectively. The colorbar is in logarithmic scale. The two dashed circles represent the cluster R_{200} and R_{500} radii equal to 1.8 Mpc and 974 kpc, respectively.

the ICM can bend the radio lobes of a radio galaxy, shaping the well-known head-tail radio galaxies (see e.g., Ryle & Windram 1968). Radio phoenixes form instead when the Active Galactic Nucleus (AGN) activity ceases and the non-thermal component is compressed (Enßlin & Gopal-Krishna 2001; Enßlin & Brüggén 2002).

Merging events in clusters can generate shock waves and turbulence that (re-)accelerate particles and both amplify and spread preexisting magnetic fields (Markevitch & Vikhlinin 2007). This non-thermal component in the ICM can give rise to diffuse synchrotron sources not associated with optical galaxies, namely, radio halos and relics. Radio halos are Mpc-scale emission located at the cluster center, while radio relics are usually found in the cluster outskirts. In some cases, however, radio relics have been observed close to the cluster center. An example is the “chair” relic in MACS J0717.5+3745 (see e.g., Bonafede et al. 2018; Rajpurohit et al. 2022). Some radio relics show a spatial connection with the lobes of a radio galaxy (Bonafede et al. 2014; Shimwell et al. 2015; van Weeren et al. 2017; Stuardi et al. 2019; HyeongHan et al. 2020), suggesting that radio relics may be powered by a re-accelerated electron population rather than an electron population being accelerated directly from the thermal pool.

Multiwavelength radio observations are crucial to classifying radio sources. Indeed, they allow us to better understand the structure of these sources as well as what is triggering the observed emission (either merging phenomena, compression, AGN, etc.) and therefore obtain important hints surrounding a cluster’s physics. For example, radio relics usually show a spectral index gradient perpendicular to the shock front (i.e., the relic elongation if the relic is seen edge-on), while head-tail radio galaxies have a flat spectral index at the core location and steeper values along the lobes as particles age. Optical and X-ray data can be used to complement the view on the cluster and cluster source physics by revealing the presence of substructures. Moreover, since radio relics are typically triggered by shock waves, sharp discontinuities in the X-ray images (in particular in the surface brightness, temperature, density, and pressure) can help

identify these kinds of sources. Conversely, cold fronts correspond to a discontinuous drop in temperature across the interface paired with a jump in density but not in pressure (as in shocks), and they are often observed bounding minihalos (see e.g., Mazzotta et al. 2001b,a; Mazzotta & Giacintucci 2008; Ghizzardi et al. 2010; Rossetti et al. 2013). However, emerging evidence from deep observations with the SKA Pathfinders and Precursors has complicated our understanding, with some minihalos extending far beyond the boundaries of known cold fronts (e.g., Biava et al. 2021; Riseley et al. 2022b).

In this paper, we report the results of a detailed multifrequency analysis of the galaxy cluster Abell 3718 (hereafter, A3718; R.A. 20h55m51.5s, Dec. $-54^{\circ}55'12''$, $z=0.139$). The cluster has a mass of $M_{500} = 3.01 \times 10^{14} M_{\odot}$ and a radius of $R_{500} = 974$ kpc (Piffaretti et al. 2011), that is, the radial distance from the cluster center at which the cluster density is 500 times the critical density of the Universe. This cluster has remained poorly studied in the literature. Thus, we present and analyze the first available radio observations of this cluster. Our new observations allow us to detect peculiar extended radio emission in this cluster for the first time, covering a projected distance of ~ 612 kpc.

The A3718 cluster was observed with the Australian SKA Pathfinder (ASKAP; McConnell et al. 2016; Hotan et al. 2021) at 943 MHz as part of the Evolutionary Map of the Universe (EMU; Norris et al. 2011) survey. In particular, observations took place during the EMU Phase I Pilot Survey (Norris et al. 2021) performed in ASKAP Band 1 and centered on a frequency of 947 MHz. The full EMU survey will conduct a census of the radio continuum source population across the (predominantly) southern sky and is predicted to detect up to about 70 million radio sources (Norris et al. 2011). The left panel of Figure 1 shows the 943 MHz EMU image in colors and contours. The same sky area was observed by ASKAP in Band 2 at a central frequency of 1367 MHz during the Phase I Pilot Survey of the Polarisation Sky Survey of the Universe’s Magnetism (POSSUM; Gaensler et al. 2010). The corresponding image is shown on the right of Figure 1. The goal of POSSUM is to investigate the magnetic

fields in the Milky Way as well as in galaxies, in clusters, and in the overall intergalactic medium. Both surveys detected the extended radio emission, although the full extent was not recovered in the POSSUM image due to its lower signal-to-noise ratio.

With its large field of view, high resolution, and good sensitivity to extended, low-surface brightness emission, ASKAP is ideally suited to performing detailed studies of galaxy clusters and, indeed, has already had significant impact in the field (e.g., HyeongHan et al. 2020; Wilber et al. 2020; Anderson et al. 2021; Brügggen et al. 2021; Reiprich et al. 2021; Di Mascolo et al. 2021; Duchesne et al. 2021a,b,c; Veronica et al. 2022; Venturi et al. 2022; Loi et al. 2022; Riseley et al. 2022a). Such studies have revealed new insights into diffuse radio sources in galaxy clusters that have furthered — and in many cases strongly challenged — our understanding of the physics of the ICM.

In this work, we aim to determine the nature of the peculiar extended radio emission and, in particular, of the thin radio arc. The morphology of the radio arc suggests two possible interpretations: the radio source is either a radio relic caused by a spherical shock wave or a tail associated with a radio galaxy possibly shaped by interactions with the ICM.

The paper is organized as follows. Optical and X-ray data and images are presented in Section 2. In Section 3, we show the radio data and images from EMU and POSSUM as well as follow-up observations performed with the Australia Telescope Compact Array (ATCA; Frater et al. 1992) at 5.5 GHz and 9 GHz. Our X-ray analysis is presented in Section 4. In Section 5, we analyze the spectral properties of the radio sources. In Section 6, we discuss the results, and in Section 7 we report our conclusions. Throughout the paper we assume a flat Λ CDM cosmology with $H_0 = 67.4$ km/s/Mpc, $\Omega_M = 0.315$ and $\Omega_\Lambda = 0.685$ (Planck Collaboration et al. 2020). At the cluster redshift (i.e., $z = 0.139$), an angular scale of 1 arcsec corresponds to a physical distance of 2.54332 kpc.

2. Optical and X-ray data and images

Information about the dynamical state of a cluster can be inferred from the analysis of the cluster galaxies and of the X-ray emission associated with the ICM. In what follows we present the optical and the X-ray data and images used to constrain the cluster's dynamical state.

2.1. Optical data and images

We searched the literature for galaxies belonging to A3718. We found five galaxies whose spectroscopic redshifts suggest that they are fiducial cluster members. These galaxies are identified in Figure 2, which shows a superposition of the Dark Energy Survey (DES) image, the X-ray emission (see next section), and the EMU image. We found two additional likely cluster-member galaxies in the DES (Abbott et al. 2021) based on the corresponding photometric redshifts.

Since we had only five cluster-member galaxies with measured spectroscopic redshifts, we instead used the DES photometric redshifts to search for the presence of substructures in A3718. We constructed our catalog by selecting the galaxies in the A3718 field that have photometric redshifts in the range $0.08 < z_{\text{phot}} < 0.18$ and uncertainties $\Delta z_{\text{phot}} \leq 0.05$. We then applied the Voronoi tessellation and percolation (VTP) procedure to this catalog (e.g., Ramella et al. 2001; Barrena et al. 2005). The VTP is a nonparametric technique that is sensitive to galaxy structures of any shape and symmetry. The VTP detected A3718

as a unique, statistically significant galaxy overdensity (at the 99.9% c.l.; 46 galaxies assigned to the cluster) with no hint of substructures in the plane of the sky. However, we cannot exclude the possibility that the cluster has a substructure along the line of sight, as we did not have a large sample of spectroscopically confirmed cluster-member galaxies with which to explore this possibility.

2.2. X-ray data and images

At X-ray wavelengths, A3718 was observed with *XMM-Newton* with a total exposure time of 43 ks (ObsID:0675010901). The observation was performed in full-frame mode for the Metal Oxide Semi-conductor (MOS) cameras and extended full-frame mode for the pn detector, all using the thin filter. Although the target of the observation was the galaxy cluster SPT-CL J2056–5459 (a cluster at redshift $z = 0.72$) and A3718 is located 9 arcmin off axis, the data are sufficient for a good characterization of the X-ray emission associated with A3718.

We retrieved the observation data files and reprocessed them with the *XMM-Newton* Science Analysis System (SAS) v19.0.0. We used tasks "emchain" and "epchain" to generate calibrated event files from the raw data. Throughout the analysis, we only used events with PATTERN<13 for MOS data and with PATTERN<5 for pn data. In addition, for all cameras, we excluded all events next to Charged Coupled Device (CCD) edges and bad pixels (i.e., FLAG==0).

The data sets were then cleaned for periods of high background due to soft protons following the two-stage filtering process described in Lovisari et al. (2011). To briefly summarize, we first extracted a light curve with bins of 100 s bins in the 10–12 (12–14) keV energy band for MOS (pn) and fitted a Poisson distribution to the histogram of this light curve. We then excluded all the time intervals deviating by more than 2σ from the mean of the distribution. The new event lists were then refiltered in a second pass as a safety check for possible flares with soft spectra (e.g., De Luca & Molendi 2004). In this case, each light curve was made with 10 s bins in the full 0.3–10 keV band. The remaining exposure times after cleaning were ~ 40 ks for MOS and ~ 30 ks for pn. Point-like sources were detected using the task "edetect-chain" and checked by eye before excluding them from the analysis. The background event files were cleaned by applying the same PATTERN selection, flare rejection, and point-source removal used for the observation events.

The X-ray image presented in this work was obtained in the 0.3–7 keV band using data from both the MOS and pn detectors and smoothed to a resolution of 6 arcsec. From the raw image, we subtracted all the components of the background (i.e., particle and cosmic) and then applied the vignetting correction by dividing with the exposure map.

In Figure 2 we present a color composite image of A3718 from our multiwavelength data. We show an optical DES image with our *XMM-Newton* 0.3–7 keV map overlaid with our 943 MHz EMU map. From Figure 2, the cluster appears to be elongated along a NW–SE axis, with a flattening of the X-ray emission along the NW edge visible in the tighter contour spacing, potentially indicating motion of the thermal gas. We analyze this further in Section 4.

3. Radio data and images

In this section, we present the data and images obtained with ASKAP at 943 and 1367 MHz and ATCA at 5.5 and 9 GHz. All of the data are summarized in Table 1.

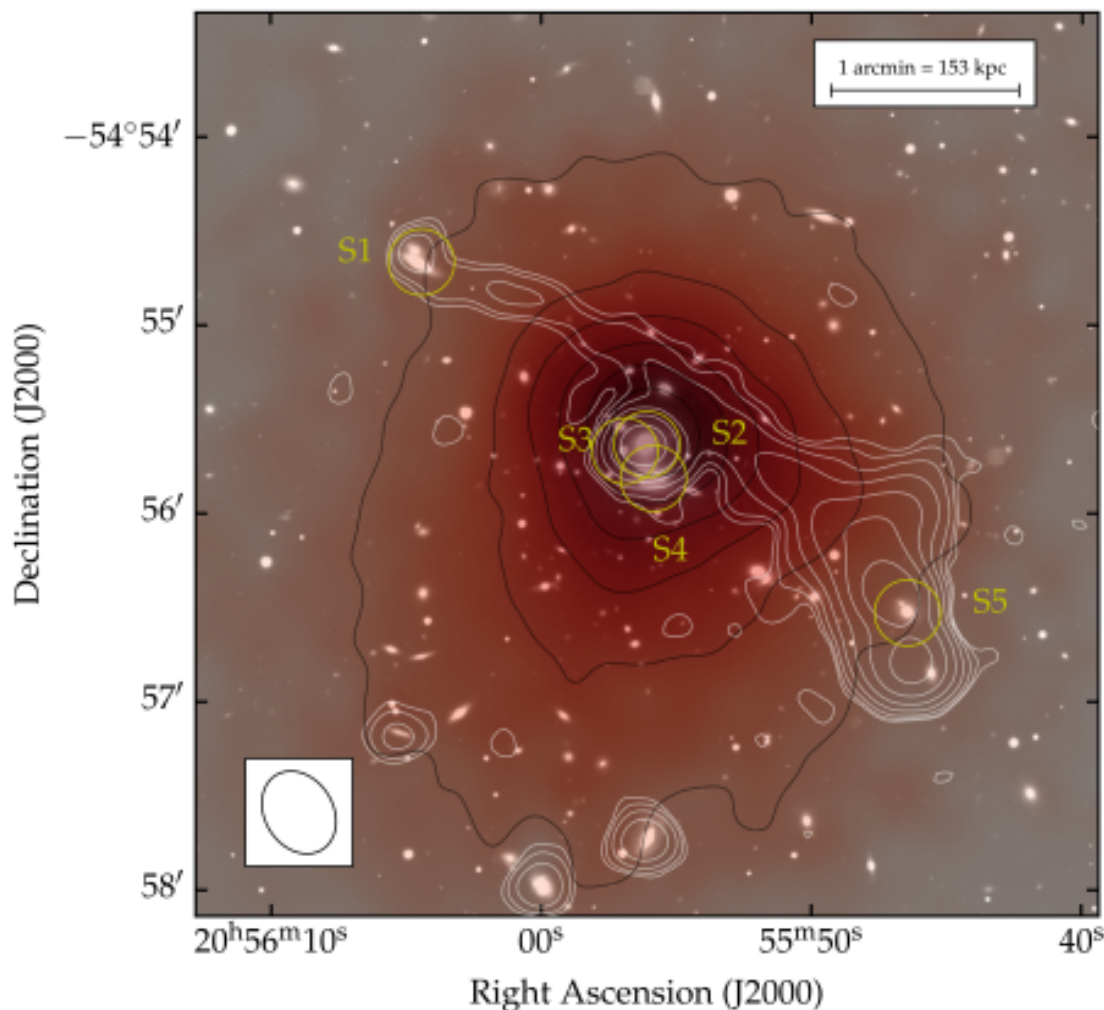


Fig. 2. Multiwavelength image of galaxy cluster A3718. The background color map shows our composite i -, r -, and g -band image from the DES. Red colors and black contours trace the X-ray surface brightness measured in the 0.3–7 keV range by *XMM-Newton*, and white contours show the 943 MHz EMU total intensity surface brightness starting from 3σ with $\sigma=40\ \mu\text{Jy}/\text{beam}$ and increasing by a factor of $\sqrt{2}$. See the text for more details.

Table 1. Summary of radio observations.

central freq. [GHz]	BW [GHz]	Instrument	uv -min	rms	res. [arcsec ²]
0.943	0.288	ASKAP-EMU	69λ	$40\ \mu\text{Jy}/\text{beam}$	13.96×10.89
1.367	0.144	ASKAP-POSSUM	100λ	$30\ \mu\text{Jy}/\text{beam}$	10×7.56
5.5	2	ATCA	1118λ	$7\ \mu\text{Jy}/\text{beam}$	1.656×3.364
9.0	2	ATCA	1830λ	$6\ \mu\text{Jy}/\text{beam}$	1.069×2.255

3.1. ASKAP data and images

The EMU and POSSUM observations used in this work have the following ASKAP Scheduling Block IDs (SBIDs): SBID 9351 and SBID 9975, respectively. Fully (direction-independent) calibrated mosaic images were downloaded through the Commonwealth Scientific and Industrial Research Organisation (CSIRO) ASKAP Science Data Archive (CASDA; Chapman et al. 2017; Huynh et al. 2020) portal¹. The EMU² data cover the frequency range between 800 MHz and 1088 MHz, while

the POSSUM³ data are between 1295 MHz and 1439 MHz. Data reduction was performed using the ASKAPSOFT pipeline (Guzman et al. 2019).

As can be seen in Figures 1 and 2, the long radio emission appears to connect (in projection) the northern cluster member S1 with the southern cluster galaxy S5 and beyond, covering a

¹ EMU: images and visibilities. v1. CSIRO. Data Collection. <http://hdl.handle.net/102.100.100/164553?index=1>

² EMU data: Norris, Ray; Filipovic, Miroslav; Huynh, Minh; Hotan, Aidan; Rudnick, Lawrence; Manojlovic, Perica; Gurkanuygun, Gulay; Parkinson, David; Macgregor, (2019): ASKAP Data Products for Project AS101 (ASKAP Pilot Survey for POSSUM): images and visibilities. v1. CSIRO. Data Collection. <http://hdl.handle.net/102.100.100/326209?index=1>

¹ <https://research.csiro.au/casda/>

² EMU data: Norris, Ray; Filipovic, Miroslav; Huynh, Minh; Hotan, Aidan; Rudnick, Lawrence; Manojlovic, Perica; Gurkanuygun, Gulay; Parkinson, David; Macgregor, (2019): ASKAP Data Products for Project AS101 (ASKAP Pilot Survey for

projected distance of ~ 612 kpc. The two bright peaks in the radio surface brightness close to the galaxy S5 (R.A. 313.94358 deg, Dec. -54.94225 deg) could be two radio lobes associated with the galaxy. This radio galaxy covers a distance of ~ 200 kpc. The length of the faint arc is ~ 370 kpc. Its width decreases going from SW to NE, from ~ 13 arcsec to 8 arcsec, and it reaches a minimum of ~ 6.5 arcsec. These scales correspond to 33, 21, and 16 kpc, respectively, and are below the beam size. It is therefore possible that we are detecting only the tip of the arc emission, which could indeed be wider than what is observed in the EMU image. The faint arc is not completely retained at higher frequency in the POSSUM image.

The extended radio emission is therefore composed of three main structures. The first is a compact radio galaxy associated with S1. The second structure is a southern radio galaxy associated with S5, which we will henceforth refer to as "S5RG", and the third is a faint radio arc connecting the two structures in projection. The radio arc is ~ 30 kpc from the X-ray peak. An additional structure was clearly detected in both images extending from the radio galaxy S5RG toward the northwest of A3718. We suggest that this structure could be a radio jet that failed to expand or faded away due to energy losses. Another possibility is that the radio jet bends toward the Earth, making it undetectable.

3.2. ATCA data and images

Higher-resolution observations were required to attempt to determine whether there is any association between the extended radio arc detected at 943 MHz and the southern radio galaxy S5RG. We carried out this investigation using the ATCA, with observations centered on S5, as the steep spectrum observed between 943 MHz and 1367 MHz (see Section 5) implied that the surface brightness would be extremely faint and challenging to recover at ATCA frequencies.

3.2.1. Data reduction

We observed S5RG during semester 2021OCT (Code C3440, P.I. F. Loi) using the 4 cm band receiver system (4.9–10.9 GHz) with three complementary array configurations (6A, 1.5C, and H168) to ensure we achieved high resolution while maintaining sensitivity to angular scales corresponding to the structures measured from the EMU and POSSUM data. We used the standard reference frequencies of 5.5 and 9 GHz for our 4 cm band observations; at each reference frequency, the Compact Array Broadband Backend (CABB; Wilson et al. 2011) provides a bandwidth of 2048 MHz at a standard 1 MHz spectral resolution. The total observing time was of the order of 30 hours evenly divided between the three configurations. Each observing run included scans of the primary bandpass and flux density calibrator PKS B1934–638 and of the phase calibrator J2040–5735.

All data reduction and imaging was performed with the MIRIAD software package (Sault et al. 1995), with calibration performed independently on each of the two intermediate frequency bands using standard techniques. The radio frequency interference environment of the ATCA 4 cm band is remarkably clean, and the flagging fraction was around 18%.

We imaged the total intensity data using a 6000 pixel grid with a pixel size of 0.4 arcsec. The final resolution of the 5.5 GHz and 9.0 GHz maps are 1.7 arcsec \times 3.4 arcsec with bpa=89 deg and 1.1 arcsec \times 2.3 arcsec with bpa=89 deg, respectively. After initial imaging, we performed four rounds of phase-only self-calibration using solution intervals of five minutes for the first

round, two minutes in the second round, and one minute for each of the last two rounds of self-calibration.

The Q and U Stokes data were imaged with a 6000 pixel grid and a pixel size of 0.4 arcsec. From these data, we derived the polarized intensity and angle images. We also derived maps of the Faraday rotation measure (RM) by fitting the polarization angle against λ^2 using the MIRIAD function IMRM.

3.2.2. Total intensity images

Figure 3 presents color composite images with the DES image in gray scale, our ATCA maps at 5.5 GHz and 9.0 GHz overlaid in color, and the 943 MHz EMU surface brightness. The two ATCA images have a beam resolution of 1.656×3.364 arcsec² and 1.069×2.255 arcsec² with BPA=89.2 deg and 89.6 deg, respectively, and a noise $\sigma=7$ μ Jy/beam and $\sigma=6$ μ Jy/beam, respectively.

Our ATCA data support the interpretation that the two surface brightness peaks seen in the ASKAP EMU and POSSUM maps are in fact the lobes of a radio galaxy associated with the cluster-member galaxy S5, which we previously referred to as S5RG. Our ATCA maps clearly reveal the structure of this radio galaxy, which is composed of a pair of radio lobes. Additionally, a compact radio counterpart to the optical galaxy is visible in our 9 GHz map due to the higher resolution; at 5.5 GHz, this compact counterpart blends into the northern lobe.

The northern lobe appears to extend further to the north in the direction of the extended tail and arc-like emission. This supports the interpretation that the faint radio arc seen at 943 MHz is connected to the radio galaxy S5RG. The southern lobe extends toward the southwest before bending to the east and again to the northeast, also following the direction of the arc.

One further intriguing feature revealed by our high-resolution ATCA data is that the northern lobe appears to show a forked tail toward its northernmost extremity. One fork is aligned with the northeast, in the direction of the extended arc, whereas the other fork appears to extend north-northwest, in the direction of emission seen by ASKAP at lower frequencies. Magnetized filamentary structures in the ICM have been detected in a number of cases (see for example Rudnick et al. 2022; Giacintucci et al. 2022; Condon et al. 2021; Fanaroff et al. 2021). The underlying magnetic field structure is modified, and the magnetic field line is stretched by physical mechanisms not yet completely understood (Yusef-Zadeh et al. 2022).

3.2.3. Polarization and rotation measure images

We made images of the linear polarization at 5.5 and 9.0 GHz convolving the Stokes Q and U images to a circular beam of 5 arcsec. Figure 4 shows the linearly polarized emission with polarization vectors overlaid and rotated by 90 degrees to indicate the direction of the magnetic field and the length of the vectors proportional to the fractional polarization. A vector polarized at 100% is shown in the top-left of the figure for reference. We also included the total intensity contours. To make these images, we considered the signal with a S/N>4 in polarized intensity and a S/N>3 in total intensity. The median and standard deviation of the fractional polarization at 9.0 GHz are $\sim 21\%$ and $\sim 23\%$, respectively.

At 5.5 GHz and 9.0 GHz, the vectors should provide a very close indication of the intrinsic magnetic field orientation since Faraday rotation is negligible as $\lambda^2 \ll 1$. Indeed, the linearly polarized emission from cluster-embedded and background ra-

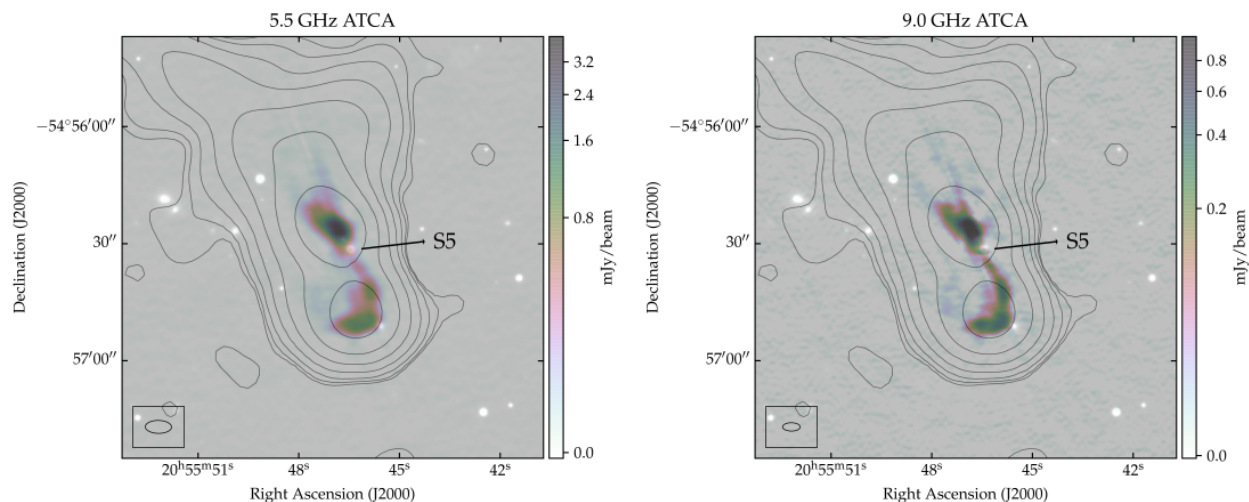


Fig. 3. ATCA total intensity images of the S5RG. Left: 5.5 GHz image with a beam resolution of 1.656×3.364 arcsec² and BPA=89.2 deg. Right: 9.0 GHz image with a beam resolution of 1.069×2.255 arcsec² and BPA=89.6 deg. In both the images we show the 943 MHz EMU image in gray contours, the DES image in gray scale colors, and the beam sizes in the bottom left-corner.

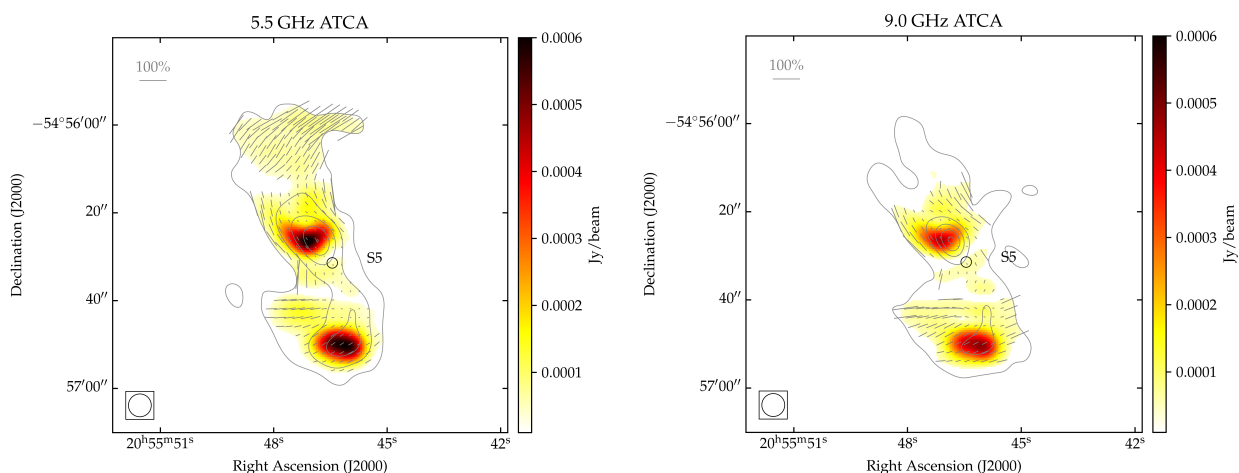


Fig. 4. ATCA linearly-polarization images of the S5RG. Left: 5.5 GHz image. Right: 9.0 GHz image. In both panels we use segments to show the intensity and the orientation of the B-field vectors. A segment with fractional polarization equal to 100% is shown in the top-left corner of the images for reference. We also overlaid the total intensity contours starting from $42 \mu\text{Jy}/\text{beam}$ and increasing by a factor of $\sqrt{2}$. All of the images have a beam resolution of 5 arcsec, shown in the bottom-left corner.

dio sources undergoes Faraday rotation from the magneto-ionic medium that is the ICM. The polarization angle rotates as a function of wavelength according to $\Delta\Psi = \text{RM} \times \lambda^2$, where $\Delta\Psi$ is the observed rotation and RM is the rotation measure. The RM is defined as the path integral of the magnetic field times the thermal particle density along the path between the emitted signal and the telescope. In the ATCA images, the vectors should provide a close indication of the intrinsic magnetic field orientation, even without correction for the local RM. A value of $|\text{RM}| = 100 \text{ rad}/\text{m}^2$, which is higher than we observed, would cause rotations of ~ 6 and ~ 17 degrees at 9.0 GHz and 5.5 GHz, respectively.

At both 5.5 GHz and 9.0 GHz, the magnetic field vectors of the northern lobe of the radio galaxy are aligned with the direction of the associated lobe or jet. Further to the north, where the tail forks, the eastern part of the fork (which aligns with the larger-scale arc) keeps the same magnetic field orientation, whereas the western part of the fork exhibits a transverse mag-

netic field orientation. This could suggest helical structure within the magnetic field. At the southern lobe location, an abrupt change in the magnetic field orientation can be observed and after that an alignment along the east-west direction.

Figure 5 shows the map of the RM obtained from our ATCA images at 5.5 GHz and 9.0 GHz. We observed negative RM values on the northern lobe and positive RMs on the southern lobe, with weighted averages of $(-20 \pm 14) \text{ rad}/\text{m}^2$ and $(+63 \pm 10) \text{ rad}/\text{m}^2$, respectively. The errors represent the weighted errors in the averages, and we did not detect any significant scatter within each lobe above that expected from the noise. The Galactic RM at this location is $(+36 \pm 8) \text{ rad}/\text{m}^2$ (Hutschenreuter et al. 2022)⁴. The average RMs of the two lobes differ significantly from this Galactic RM value, indicating likely contributions from the ICM.

⁴ Using the CIRADA RM cutout server at <http://cutouts.cirada.ca/rmcutout/>

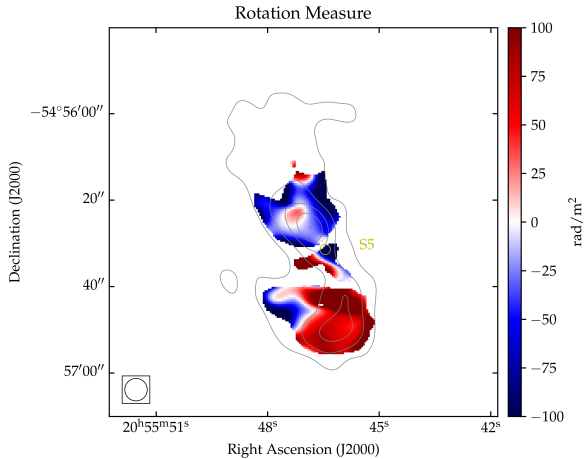


Fig. 5. Rotation measure image computed from 5.5 GHz and 9.0 GHz ATCA data.

4. X-ray analysis

In this section, we present a detailed analysis of our *XMM-Newton* data to investigate whether the properties of the radio arc are being influenced by the ICM. In particular, the X-ray asymmetry will be better investigated.

4.1. X-ray asymmetry

The X-ray asymmetry observed in Figure 2 is better shown in Figure 6. On the right of Fig. 6, we show the soft X-ray surface brightness (in the 0.7 to 2 keV range) profiles toward the NW and SE starting from the X-ray peak. The equal radius regions are shown on the left and are overlaid on the X-ray surface brightness image. Figure 2 shows that the X-ray surface brightness profile is steeper toward the NW (in the direction of the radio arc) than toward the SE. Moreover, we know that the Sunyaev-Zeldovich SZ emission is not coincident with the brightest cluster galaxy (BCG) position, and the BCG and the SZ peak are at a projected distance of ~ 130 kpc along the NW. We should also note that the peak of the X-ray emission is closer to the BCG (~ 12 kpc). In addition, we measured a metallicity of $Z \sim 1.0$ at $R < 75$ kpc $\approx 0.08R_{500}$, a concentration of $c \sim 0.1$, and a centroid shift of $w = 7.2 \cdot 10^{-3}$. These values are consistent with the typical values observed for relaxed clusters (e.g., Mernier et al. 2018, Lovisari & Reiprich 2019, Lovisari et al. 2017).

The conclusion about A3718 being a relaxed cluster would favor the second hypothesis made in the introduction: The radio arc could be a tail associated with S5RG. The shape of the arc could be due to the motion of the host galaxy S5 in the ICM. Moreover, the width of the tail remains uniform along its full length, in contrast to other head-tail radio galaxies where the tail broadens, going away from the host due to adiabatic expansion (see e.g., NGC 7385 and PKS B0053-015 in Sebastian et al. 2017). Based on these observations, we explored the X-ray image further to understand whether the ICM has a role in shaping this structure.

4.2. X-ray spectral maps

We attempted to better investigate the possible interplay between the thermal gas and the radio arc through X-ray spectral maps. Following the same method used in Brienza et al.

(2022), we extracted the spectra from small regions. We used the weighted Voronoi tessellation binning algorithm by Diehl & Statler (2006), which is a generalization of the Cappellari & Copin (2003) Voronoi binning algorithm, to obtain the sizes of the spatial bins.

The resulting temperature, density, pressure, and entropy maps are shown in Figure 7 with EMU radio contours. All of the images highlight the X-ray asymmetry observed in the original *XMM-Newton* image. In particular, lower values of both temperature and entropy to the NW in the region of the arc with respect to those observed on the opposite side of the cluster center can be seen. Even if these images suggest a connection between the radio arc and the ICM, we would need deeper X-ray and radio observations to understand the physics at play in this particular and intriguing case.

5. Radio spectral index analysis

The radio source spectral index behavior is a key tool for investigating the physics of a radio source and identifying where particles are injected and how they age. In this section, we derive the spectral index properties of the extended radio source.

5.1. ASKAP spectral index image

We analyzed the resolved spectral index of the radio source considering the EMU and POSSUM images at 20 arcsec. The spectral index map and uncertainty were computed as:

$$\alpha = -\frac{\log(B_1/B_2)}{\log(\nu_1/\nu_2)}, \quad (1)$$

$$\Delta\alpha = \frac{1}{\log(\nu_1/\nu_2)} \sqrt{\left(\frac{\Delta B_1}{B_1}\right)^2 + \left(\frac{\Delta B_2}{B_2}\right)^2}, \quad (2)$$

where B_1 and B_2 represent the surface brightness at frequency ν_1 and ν_2 , respectively (i.e., the EMU and POSSUM frequencies). The results are shown in Figure 8 with the EMU contours overlaid. The extended radio source shows a steepening spectral gradient along its length, from a spectral index $\alpha \approx 0.6$ at the center near S5RG to a value of $\alpha \approx 4$ at the furthest distance from S5RG (excluding regions corresponding to S1).

The spectral steepening along the arc can be better appreciated by examining the profile in subregions. This is presented in Figure 9, where we derived the spectral index using the integrated flux density of our EMU and POSSUM maps. The profile shown in Fig. 9 echoes the behavior seen in the maps presented in Figure 8. Considering the spectral index trend along the arc and assuming that the cluster is relaxed, it is possible that the arc is indeed a tail associated with the S5 galaxy.

We note that the northern cluster galaxy, S1, appears to show a spectral index gradient toward the center, from a value of $\alpha \approx 0.8$ to $\alpha \approx 3$ and with a typical uncertainty $\Delta\alpha \lesssim 1$. Due to the steep-spectrum nature of the tail and the fact that these components are blurred in our EMU maps but not in our POSSUM maps, we suggest that this apparent gradient could be the result of blending between radio emission associated with S1 and the arc.

Finally, we also note that the BCG region has a steep spectral index of 1.5 at the peak of the surface brightness and flatter values toward northwest and southeast, where we measure a spectral index of about one. This spectral index behavior could be due to the blending of the central cluster sources.

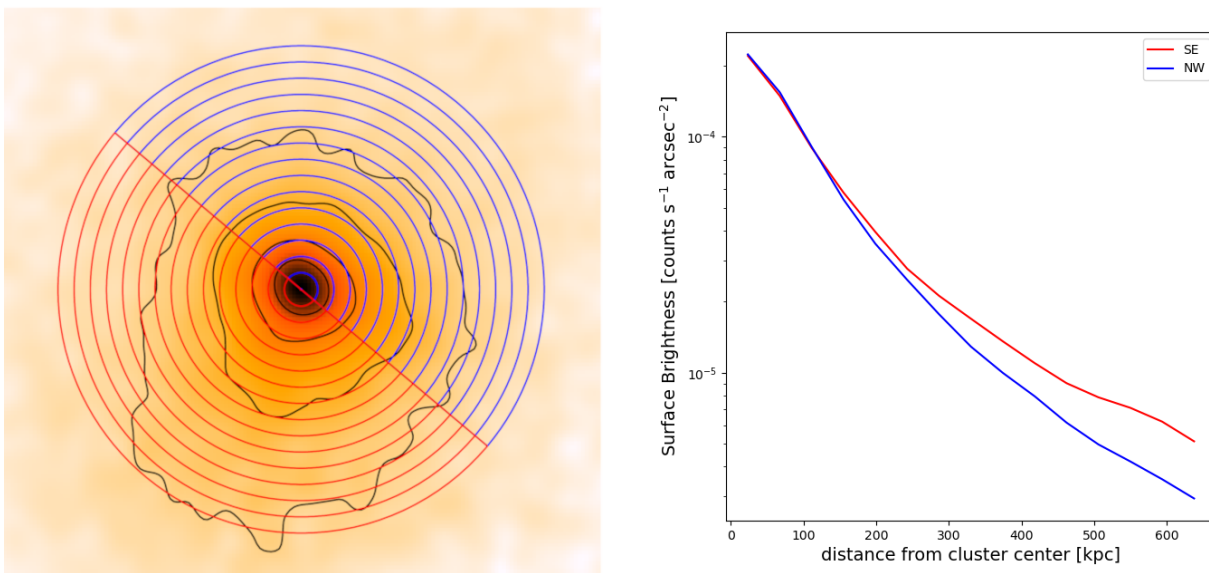


Fig. 6. X-ray surface brightness image and profile. Left: X-ray surface brightness image between 0.2-7 keV in colors and with contours. Green and red annuli start from the brightest peak of emission and extend toward the NW and SE, respectively. The inclination of the sectors is perpendicular to the radio arc. Right: X-ray surface brightness profiles corresponding to NW and SE annuli in same color code.

5.2. ATCA spectral index image

The interpretation proposed in the previous section seems consistent with the spectral index image made between 5.5 and 9.0 GHz after convolving the ATCA images to a common resolution of 5 arcsec with a circular beam. The results of this process are shown in Figure 10.

The spectral index steepens as the distance from S5 increases both the north and the south. This strongly supports our hypothesis that S5 is the host of the radio emission S5RG. To the south, the spectral steepening follows the morphology of the radio emission, as the spectral index is increasingly steep along the presumed axis of the jet or lobe as it travels south before bending to the east and then northeast.

It is important to note that the western structure of the fork tail shows a flat spectral index of about 0.5. Although the associated error is quite large (~ 1.6), we can argue that some mechanism is reenergizing the particles in this region, maybe the same mechanism that is shaping the western structure.

6. Summary and discussion

In this paper, we conducted a multifrequency study of the galaxy cluster A3718. This far southern cluster, at a declination of -54 degrees, has been poorly studied so far, and no previous radio frequency studies are present in the literature. Our interest was triggered by a radio arc located near the cluster center and detected for the first time during the EMU Phase I Pilot Survey. The radio arc, due to its morphology, could be either a radio relic or a tail associated with a radio galaxy.

Optical and X-ray data suggest that the cluster is in a relaxed dynamical state, which is consistent with the interpretation reported by Zenteno et al. (2020). These authors carried out a joint SZ, X-ray, optical analysis of the dynamical state of 288 massive galaxy clusters. In particular, they concluded that A3718 (which they referred to as SPT-CLJ2055-5456) is a relaxed cluster. Thus, the interpretation of the observed radio arc as being a relic is disfavored by their conclusion. Indeed, radio relics are usually found in merging clusters where shock waves can am-

plify magnetic fields and accelerate particles. However, the X-ray image shows a slight asymmetry with a flattened NW edge that could indicate an interaction with the complex radio source. Moreover, we observed a clear asymmetry in the X-ray spectral maps, suggesting that the cluster is not entirely relaxed. In particular, we note that the temperature and entropy maps show lower values NW from the X-ray peak in the region of the radio arc, while they increase in the opposite direction with respect to the X-ray peak. This asymmetry suggests a connection between the radio arc and the ICM. However, we do not have enough resolution and sensitivity to draw strong conclusions. Deeper observations with *XMM-Newton* and/or *Chandra* would be required.

By analyzing ASKAP data from the pilot EMU and POSUM surveys at 943 MHz and 1.367 GHz, respectively, and targeted ATCA observations at 5.5 GHz and 9.0 GHz, we have discovered that the radio emission observed in the EMU image is composed of a compact radio source associated with the optical galaxy S1, an arc of radio emission having a length of ~ 370 kpc and a width of ~ 25 kpc, and a southern radio galaxy (S5RG) with two lobes bending in the arc direction and extending for ~ 200 kpc. The radio arc is extremely thin. Therefore, it is possible that we are detecting only the brightest patches associated with this source.

The ASKAP and ATCA images revealed two additional intriguing structures. The first structure can be seen in the ASKAP image northeast from S5RG and seems to be a jet that either failed to expand or faded away due to energy losses. The second structure is a forked tail observed in our ATCA images toward the northwest of the northern lobe of S5RG.

The ATCA polarized intensity image shows B-vectors aligned with the direction of the lobe or jet, and this supports the picture proposed. Curiously, the western part of the fork tail shows a transverse B-field. In the RM image, we predominantly found positive/negative values associated with the southern/northern lobes of S5RG. This suggests that there is a different portion of magneto-ionic plasma in front of the lobes. One potential cause of the RM difference between the lobes could be their different distance along the line of sight, and thus the observed emission passes along different path lengths through the

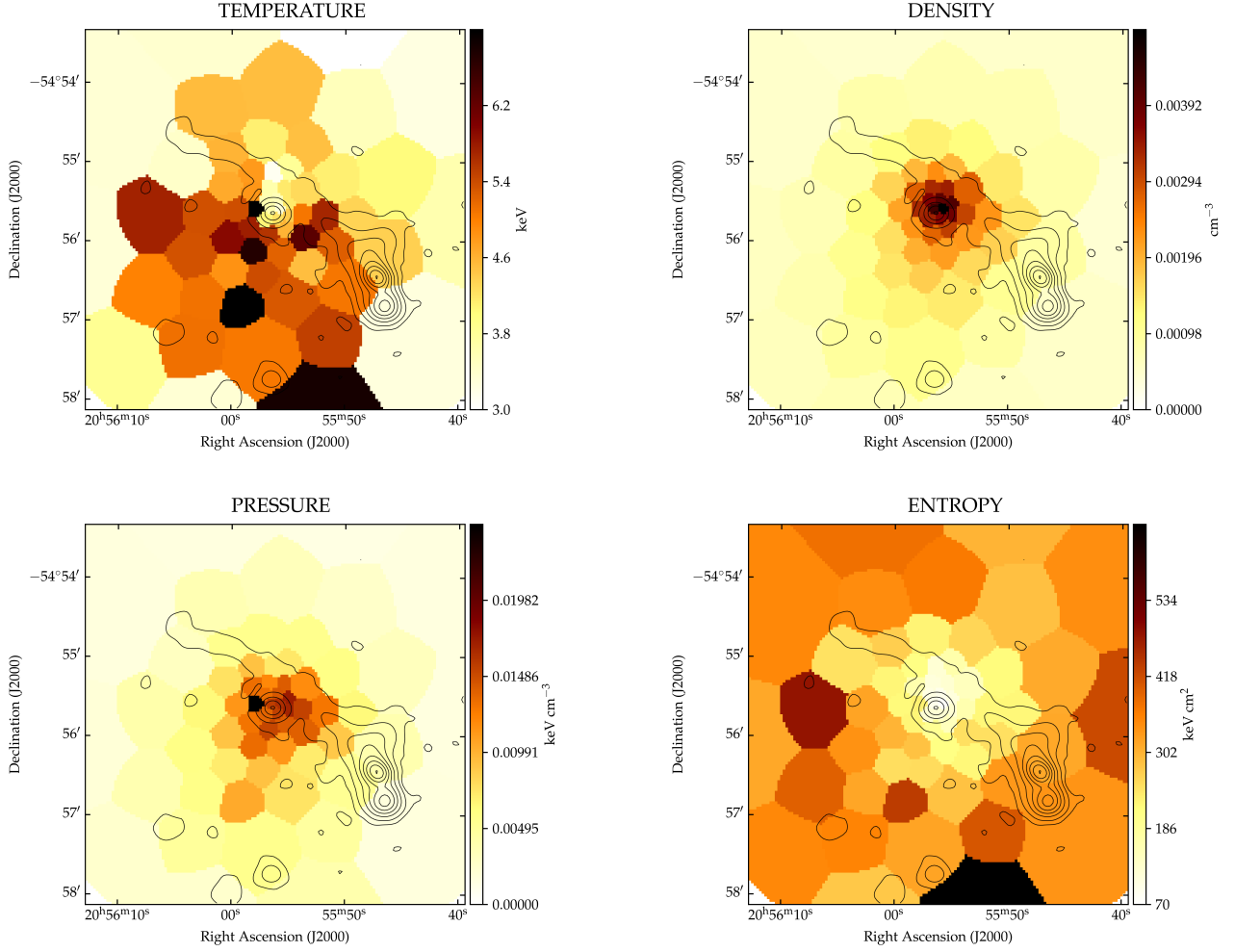


Fig. 7. Projected temperature (top-left), density (top-right), pressure (bottom-left), and entropy (bottom-right) with 943 MHz EMU contours.

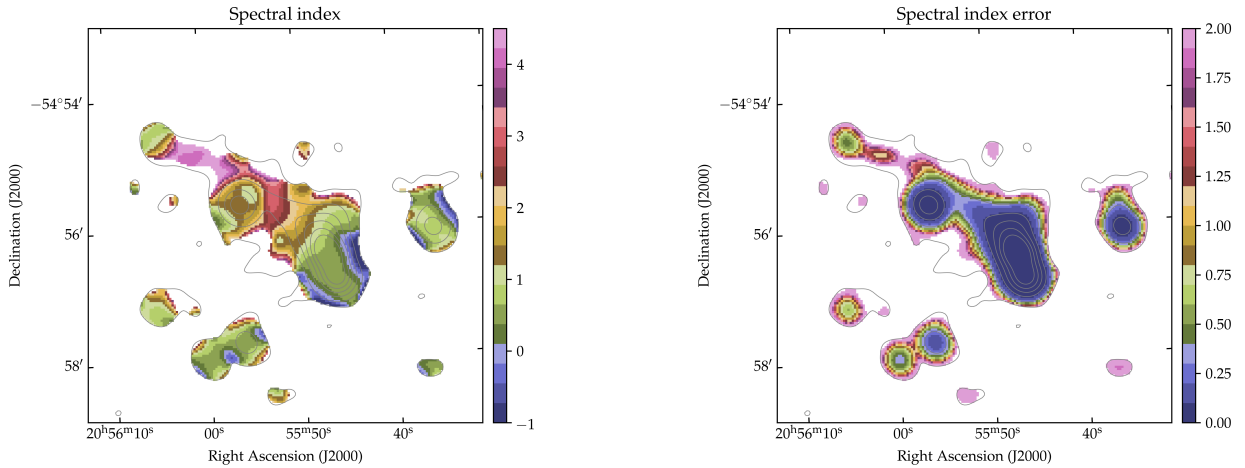


Fig. 8. ASKAP spectral index map and uncertainty map computed between 943 MHz and 1.367 GHz at 13 arcsec of resolution.

ICM. This would then imply that the radio galaxy and the arc extend for greater distances than implied by the projected 2D size.

Considering the ASKAP and ATCA spatially resolved spectral index images, the radio arc seems to be a tail associated with

S5RG. Indeed, we observe a steepening of the spectral index from the S5RG, where we measure $\alpha_{943\text{MHz}}^{1.367\text{GHz}} \approx 0.6$ along the arc. Toward the end of the arc, the spectral index reaches very steep values with $\alpha_{943\text{MHz}}^{1.367\text{GHz}} \approx 4$.

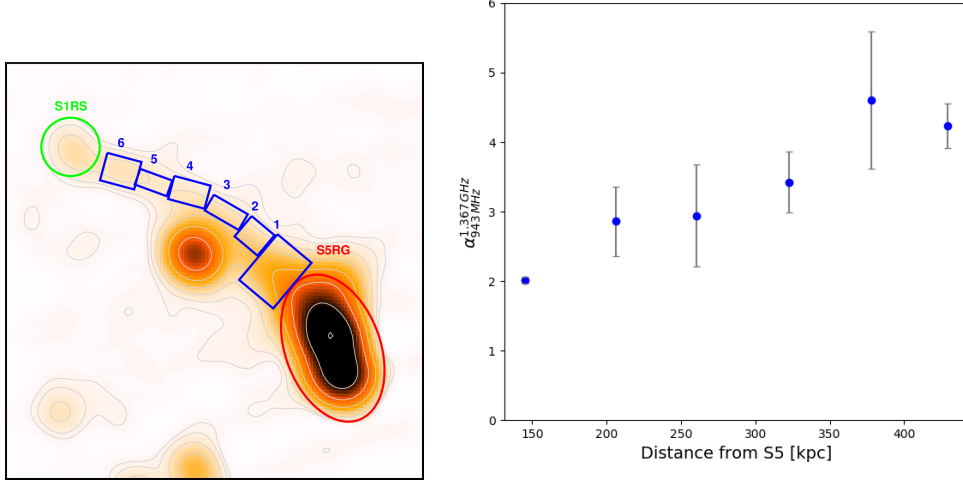


Fig. 9. Spectral index gradient along the radio arc. Left: 943 MHz EMU image. Right: ASKAP spectral index as a function of the distance from the galaxy S5 measured in the six blue boxes shown in the top image.

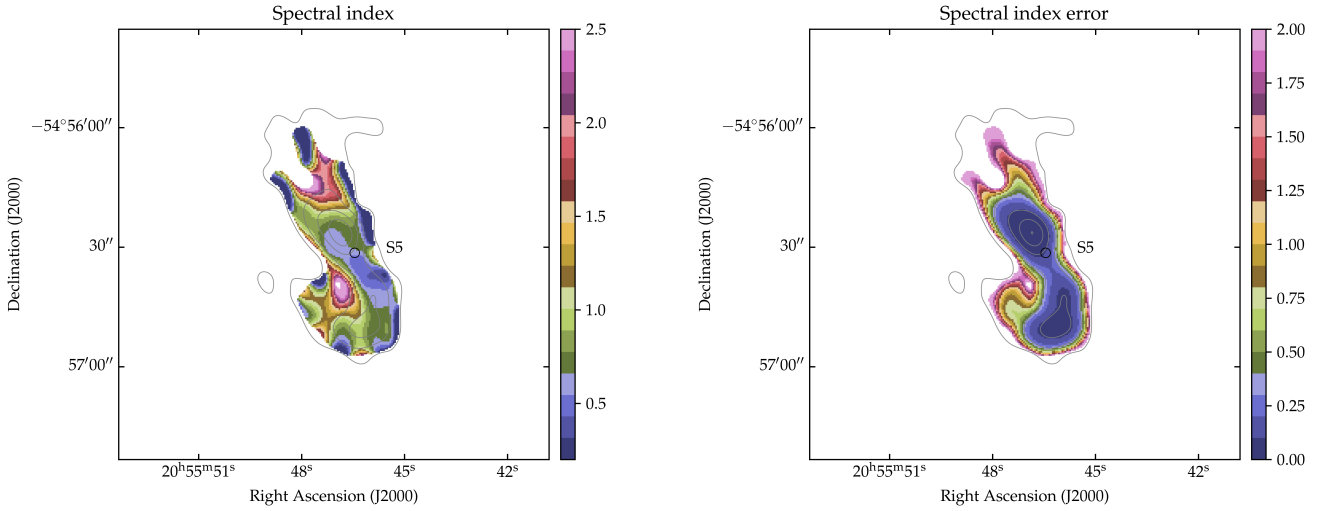


Fig. 10. ATCA spectral index map and uncertainty map computed between 5.5 GHz and 9.0 GHz at 5 arcsec of resolution.

From these results we have computed a first order estimate of the radiative age of the arc, assuming that particles age following a JP model (Jaffe & Perola 1973). Considering a magnetic field strength that minimizes the energy losses (i.e., $B=B_{\text{CMB}}/\sqrt{3} = 2.4 \mu\text{G}$) and a spectral injection index of 0.6, as measured in the region closest to the S5 galaxy in the EMU-POSSUM spectral index image, which is likely close to particle injection, we have simulated the evolution of the JP spectrum in time. According to our simulation, to observe a steepening of the spectrum up to the observed index $\alpha_{943\text{ MHz}}^{1.367\text{ GHz}} = 4$, the source age must be around 180 Myrs.

We then computed the path covered by the galaxy S5 through the ICM in this amount of time and compared it with the radio source observed length. We do not know the velocity of the galaxy, but we can assume the equipartition condition between the ICM and the galaxy energy density (see, e.g., Boschin & Giardi 2018):

$$\sigma_v^2 = (kT_X)/(\mu m_p), \quad (3)$$

where $\mu = 0.58$ is the mean molecular weight and m_p the proton mass. Given the ICM temperature of $T_X \sim 4.4 \text{ keV}$, the resulting galaxy velocity dispersion is $\sigma_v \sim 800 \text{ km/s}$. Therefore, taking this value for the velocity of the galaxy, during 180 Myrs it moved through the ICM to a distance of $l = v \cdot t = 140 \text{ kpc}$, a factor of ~ 3.3 smaller than the length of the radio arc plus the northern lobe of S5RG.

Indeed, to cover the observed distance, the galaxy S5 would need a time interval of about 600 Myrs. Such an age would imply a spectral index much steeper than the observed profile. Moreover, after this amount of time, we should not be able to detect the arc, due to its very low surface brightness. Crucially, however, we have noted that the arc is very narrow. Normally, tails associated with radio galaxies become broader due to the spontaneous adiabatic expansion of the plasma, unless some external interaction causes a recollimation (see for example Velović et al. 2022). The physical mechanism responsible for the characteristics of the observed radio arc is not clear, but we can examine three options: 1) The radio galaxy is ejecting magnetic

field and particles at such high velocity that they can cover the observed arc length. 2) Instabilities between the tail and the ICM cause turbulence that may disrupt and re-accelerate dormant tail electrons. 3) The nonthermal plasma of the arc is being re-accelerated through weak shock(s) or compression.

Jet velocities can be extremely high in radio galaxies. Laing & Bridle (2002) estimated a jet velocity for 3C31 of the order of 10^5 km/s nearby the AGN (tens of kpc). O’Neill et al. (2019) produced a magneto-hydro-dynamical simulation of a narrow-angle tail galaxy assuming jet velocity of the order of 10^4 km/s and an ICM with similar density but with a pressure higher by a factor of ten with respect to A3718. After 540 Myrs, the tails reach a length comparable to our radio source, with a steepening of the spectral index from the core along the tails. However, the spectral index steepens to a maximum of $\alpha_{950\text{MHz}}^{1.4\text{GHz}} = 2$, while in our case the spectral index at the end of the arc is significantly steeper, as we observed values up to $\alpha_{943\text{MHz}}^{1.367\text{GHz}} = 4$. A combination of the galaxy motion through the cluster and a jet velocity could be enough to explain the presence of the arc and its shape, although only dedicated numerical simulations could give us a definitive answer. Indeed, if this is the case, we would expect to see a combination of freshly injected particles and aged ones at greater distances from the hosting galaxy. This would probably result in a spectral index flatter than what we observed, as also shown in the aforementioned simulations.

The second option for explaining the physical mechanism has been proposed in several cases (de Gasperin et al. 2017; Wilber et al. 2018; Müller et al. 2021; Botteon et al. 2021; Ignesti et al. 2022). Turbulence is indeed expected in tails of radio galaxies due to the interaction with the ICM. This mechanism can re-accelerate particles and prevent their aging, causing a flattening of the spectral index, especially at greater distances from the host, where radiative losses are important. This explanation has been tentatively reported by Sebastian et al. (2017). However, even this scenario is disfavored by the observed spectral index gradient, at least at this resolution that corresponds to about 33 kpc.

The third scenario also implies a flattening of the radio spectrum. Weak shocks can reenergize high-frequency particles, while compression results in a shift of the spectrum, and both mechanisms can leave traces in the X-ray images. According to the X-ray spectral maps, we observed only a possible enhancement of the pressure, and this scenario also implies an increase in the temperature and entropy. Deeper X-ray data as well as higher-resolution radio observations at low frequencies would be required to probe this scenario further.

7. Conclusions

In this work we conducted a multifrequency study of the galaxy cluster A3718 and, in particular, of a complex radio source detected for the first time during the EMU phase I survey. The radio source appears as an extremely thin (~ 30 kpc) emission very close to the cluster center (~ 12 kpc) and extending for ~ 612 kpc. The morphology is similar to previously detected radio relic structures. However, the optical and X-ray data suggest that A3718 shows an overall relaxed morphology, which is in conflict with the general idea that radio relics trace shock waves propagating in merging clusters.

By analyzing the 943 MHz and 1.367 GHz ASKAP and the 5.5 GHz and 9.0 GHz ATCA data, both in total intensity and polarization, we concluded that the extended radio source is composed of a compact radio source in the north, a thin radio arc, and a southern radio galaxy (S5RG). The radio arc and S5RG cover a

projected distance of ~ 370 kpc and ~ 200 kpc, respectively. The radio arc is likely a tail associated with S5RG, although we did not detect a clear connection between these two structures at high resolution in our ATCA images. This is not surprising since the arc has a very steep spectral index, with $\langle \alpha_{943\text{MHz}}^{1.367\text{GHz}} \rangle = 2 - 4$, and it is very faint ($S_{943\text{MHz}} = 73 \mu\text{Jy/arcsec}^2$).

Considering the arc and the radio galaxy S5RG as a unique system, we concluded that the motion of the galaxy through the ICM is not enough to produce the observed radio length. Therefore, either the radio jet is ejected with a velocity of the order of 10^4 km/s or the arc is receiving an energy boost from the ICM. With the available data, we cannot tell whether the arc is powered by turbulence induced by instabilities between the arc and the ICM, compression, or weak shock(s). Deeper X-ray and radio observation would allow us to finally shed light on the mechanism responsible for this ultra-steep and very thin radio arc near the center of A3718.

Acknowledgements. We thank the anonymous reviewer for the useful comments and suggestions. FL acknowledges financial support from the Italian Minister for Research and Education (MIUR), project FARE, project code R16PR59747, project name FORNAX-B. FL acknowledges financial support from the Italian Ministry of University and Research – Project Proposal CIR01_00010. MB acknowledges financial support from the program UNESCO-L’Oréal Italia per le Donne nella scienza, from the ERC-Stg “DRANOEL”, no. 714245, from the ERC-Stg “MAGCOW”, no. 714196, from the agreement ASI-INAF n. 2017-14-H.O and from the PRIN MIUR 2017PH3WAT “Blackout”. AB and CJR acknowledge support from the ERC Starting Grant ‘DRANOEL’, number 714245. AB and CS acknowledges financial support from the Italian Minister for Research and Education (MIUR), project SMS. The Australian SKA Pathfinder is part of the Australia Telescope National Facility (<https://ror.org/05qajvd42>) which is managed by CSIRO. Operation of ASKAP is funded by the Australian Government with support from the National Collaborative Research Infrastructure Strategy. ASKAP uses the resources of the Pawsey Supercomputing Centre. Establishment of ASKAP, the Murchison Radio-astronomy Observatory and the Pawsey Supercomputing Centre are initiatives of the Australian Government, with support from the Government of Western Australia and the Science and Industry Endowment Fund. We acknowledge the Wajarri Yamatji people as the traditional owners of the Observatory site. The POSSUM project (<https://askap.org/possum>) has been made possible through funding from the Australian Research Council, the Natural Sciences and Engineering Research Council of Canada, the Canada Research Chairs Program, and the Canada Foundation for Innovation. The Australia Telescope Compact Array is part of the Australia Telescope National Facility (<https://ror.org/05qajvd42>) which is funded by the Australian Government for operation as a National Facility managed by CSIRO. We acknowledge the Gomeri people as the traditional owners of the Observatory site. This research has made use of the CIRADA cutout service at URL cutouts.cirada.ca, operated by the Canadian Initiative for Radio Astronomy Data Analysis (CIRADA). CIRADA is funded by a grant from the Canada Foundation for Innovation 2017 Innovation Fund (Project 35999), as well as by the Provinces of Ontario, British Columbia, Alberta, Manitoba and Quebec, in collaboration with the National Research Council of Canada, the US National Radio Astronomy Observatory and Australia’s Commonwealth Scientific and Industrial Research Organisation.

References

- Abbott, T. M. C., Adamów, M., Aguena, M., et al. 2021, *ApJS*, 255, 20
 Anderson, C. S., Heald, G. H., Eilek, J. A., et al. 2021, *PASA*, 38, e020
 Barrena, R., Ramella, M., Boschin, W., et al. 2005, *A&A*, 444, 685
 Biava, N., de Gasperin, F., Bonafede, A., et al. 2021, *MNRAS* [arXiv:2110.01629]
 Bonafede, A., Brüggén, M., Rafferty, D., et al. 2018, *MNRAS*, 478, 2927
 Bonafede, A., Intema, H. T., Brüggén, M., et al. 2014, *ApJ*, 785, 1
 Boschin, W. & Girardi, M. 2018, *MNRAS*, 480, 1187
 Botteon, A., Brunetti, G., van Weeren, R. J., et al. 2020a, *ApJ*, 897, 93
 Botteon, A., Giacintucci, S., Gastaldello, F., et al. 2021, *A&A*, 649, A37
 Botteon, A., van Weeren, R. J., Brunetti, G., et al. 2020b, *MNRAS*, 499, L11
 Brienza, M., Lovisari, L., Rajpurohit, K., et al. 2022, *A&A*, 661, A92
 Brüggén, M., Reiprich, T. H., Bulbul, E., et al. 2021, *A&A*, 647, A3
 Cappellari, M. & Copin, Y. 2003, *MNRAS*, 342, 345
 Chapman, J. M., Dempsey, J., Miller, D., et al. 2017, in *Astronomical Society of the Pacific Conference Series*, Vol. 512, *Astronomical Data Analysis Software and Systems XXV*, ed. N. P. F. Lorente, K. Shorridge, & R. Wayth, 73

- Condon, J. J., Cotton, W. D., White, S. V., et al. 2021, *ApJ*, 917, 18
- de Gasperin, F., Intema, H. T., Shimwell, T. W., et al. 2017, *Science Advances*, 3, e1701634
- De Luca, A. & Molendi, S. 2004, *A&A*, 419, 837
- Di Mascolo, L., Mroczkowski, T., Perrott, Y., et al. 2021, *A&A*, 650, A153
- Diehl, S. & Statler, T. S. 2006, *MNRAS*, 368, 497
- Duchesne, S. W., Johnston-Hollitt, M., & Bartalucci, I. 2021a, *PASA*, 38, e053
- Duchesne, S. W., Johnston-Hollitt, M., Bartalucci, I., Hodgson, T., & Pratt, G. W. 2021b, *PASA*, 38, e005
- Duchesne, S. W., Johnston-Hollitt, M., & Wilber, A. G. 2021c, *PASA*, 38, e031
- Ebeling, H., Stephenson, L. N., & Edge, A. C. 2014, *ApJ*, 781, L40
- EnBlin, T. A. & Brügger, M. 2002, *MNRAS*, 331, 1011
- EnBlin, T. A. & Gopal-Krishna. 2001, *A&A*, 366, 26
- Fanaroff, B., Lal, D. V., Venturi, T., et al. 2021, *MNRAS*, 505, 6003
- Frater, R. H., Brooks, J. W., & Whiteoak, J. B. 1992, *Journal of Electrical and Electronics Engineering Australia*, 12, 103
- Fumagalli, M., Fossati, M., Hau, G. K. T., et al. 2014, *MNRAS*, 445, 4335
- Gaensler, B. M., Landecker, T. L., Taylor, A. R., & POSSUM Collaboration. 2010, in *American Astronomical Society Meeting Abstracts*, Vol. 215, *American Astronomical Society Meeting Abstracts #215*, 470.13
- Ghizzardi, S., Rossetti, M., & Molendi, S. 2010, *A&A*, 516, A32
- Giacintucci, S., Venturi, T., Markevitch, M., et al. 2022, *ApJ*, 934, 49
- Govoni, F., Orrù, E., Bonafede, A., et al. 2019, *Science*, 364, 981
- Guzman, J., Whiting, M., Voronkov, M., et al. 2019, *ASKAPsoft: ASKAP science data processor software*, *Astrophysics Source Code Library*, record ascl:1912.003
- Hotan, A. W., Bunton, J. D., Chippendale, A. P., et al. 2021, *PASA*, 38, e009
- Hutschenreuter, S., Anderson, C. S., Betti, S., et al. 2022, *A&A*, 657, A43
- Huynh, M., Dempsey, J., Whiting, M. T., & Ophel, M. 2020, in *Astronomical Society of the Pacific Conference Series*, Vol. 522, *Astronomical Data Analysis Software and Systems XXVII*, ed. P. Ballester, J. Ibsen, M. Solar, & K. Shortridge, 263
- HyeongHan, K., Jee, M. J., Rudnick, L., et al. 2020, *ApJ*, 900, 127
- Ignesti, A., Brunetti, G., Shimwell, T., et al. 2022, *A&A*, 659, A20
- Jaffe, W. J. & Perola, G. C. 1973, *A&A*, 26, 423
- Laing, R. A. & Bridle, A. H. 2002, *MNRAS*, 336, 1161
- Loi, F., Serra, P., Murgia, M., et al. 2022, *A&A*, 660, A48
- Lovisari, L., Forman, W. R., Jones, C., et al. 2017, *ApJ*, 846, 51
- Lovisari, L. & Reiprich, T. H. 2019, *MNRAS*, 483, 540
- Lovisari, L., Schindler, S., & Kapferer, W. 2011, *A&A*, 528, A60
- Markevitch, M. & Vikhlinin, A. 2007, *Phys. Rep.*, 443, 1
- Mazzotta, P. & Giacintucci, S. 2008, *ApJ*, 675, L9
- Mazzotta, P., Markevitch, M., Forman, W. R., et al. 2001a, *arXiv e-prints*, astro
- Mazzotta, P., Markevitch, M., Vikhlinin, A., et al. 2001b, *ApJ*, 555, 205
- McConnell, D., Allison, J. R., Bannister, K., et al. 2016, *PASA*, 33, e042
- Mernier, F., Biffi, V., Yamaguchi, H., et al. 2018, *Space Sci. Rev.*, 214, 129
- Müller, A., Pfrommer, C., Ignesti, A., et al. 2021, *MNRAS*, 508, 5326
- Norris, R. P., Hopkins, A. M., Afonso, J., et al. 2011, *PASA*, 28, 215
- Norris, R. P., Marvil, J., Collier, J. D., et al. 2021, *PASA*, 38, e046
- O'Neill, B. J., Jones, T. W., Nolting, C., & Mendygral, P. J. 2019, *ApJ*, 884, 12
- Piffaretti, R., Arnaud, M., Pratt, G. W., Pointecouteau, E., & Melin, J. B. 2011, *A&A*, 534, A109
- Planck Collaboration, Aghanim, N., Akrami, Y., et al. 2020, *A&A*, 641, A6
- Rajpurohit, K., Hoft, M., Wittor, D., et al. 2022, *A&A*, 657, A2
- Ramella, M., Boschin, W., Fadda, D., & Nonino, M. 2001, *A&A*, 368, 776
- Reiprich, T. H., Veronica, A., Pacaud, F., et al. 2021, *A&A*, 647, A2
- Riseley, C. J., Bonnassieux, E., Vernstrom, T., et al. 2022a, *MNRAS*, 515, 1871
- Riseley, C. J., Rajpurohit, K., Loi, F., et al. 2022b, *MNRAS*, 512, 4210
- Rossetti, M., Eckert, D., De Grandi, S., et al. 2013, *A&A*, 556, A44
- Rudnick, L. 2021, *Galaxies*, 9, 85
- Rudnick, L., Brügger, M., Brunetti, G., et al. 2022, *ApJ*, 935, 168
- Ryle, M. & Windram, M. D. 1968, *MNRAS*, 138, 1
- Sault, R. J., Teuben, P. J., & Wright, M. C. H. 1995, in *Astronomical Society of the Pacific Conference Series*, Vol. 77, *Astronomical Data Analysis Software and Systems IV*, ed. R. A. Shaw, H. E. Payne, & J. J. E. Hayes, 433
- Sebastian, B., Lal, D. V., & Pramesh Rao, A. 2017, *AJ*, 154, 169
- Shimwell, T. W., Markevitch, M., Brown, S., et al. 2015, *MNRAS*, 449, 1486
- Smith, R. J., Lucey, J. R., Hammer, D., et al. 2010, *MNRAS*, 408, 1417
- Stuardi, C., Bonafede, A., Wittor, D., et al. 2019, *MNRAS*, 489, 3905
- van Weeren, R. J., Andrade-Santos, F., Dawson, W. A., et al. 2017, *Nature Astronomy*, 1, 0005
- van Weeren, R. J., de Gasperin, F., Akamatsu, H., et al. 2019, *Space Sci. Rev.*, 215, 16
- Velović, V., Filipović, M. D., Barnes, L., et al. 2022, *MNRAS*, 516, 1865
- Venturi, T., Giacintucci, S., Merluzzi, P., et al. 2022, *A&A*, 660, A81
- Veronica, A., Su, Y., Biffi, V., et al. 2022, *A&A*, 661, A46
- Wilber, A., Brügger, M., Bonafede, A., et al. 2018, *MNRAS*, 473, 3536
- Wilber, A. G., Johnston-Hollitt, M., Duchesne, S. W., et al. 2020, *PASA*, 37, e040
- Wilson, W. E., Ferris, R. H., Axtens, P., et al. 2011, *MNRAS*, 416, 832
- Yusef-Zadeh, F., Arendt, R. G., & Wardle, M. 2022, *arXiv e-prints*, arXiv:2210.04913
- Zenteno, A., Hernández-Lang, D., Klein, M., et al. 2020, *MNRAS*, 495, 705